

• Original Paper •

Responses of Mean and Extreme Precipitation to Different Climate Forcing Under Radiative-Convective Equilibrium

Chenyu MA¹, Wei YUAN², and Ji NIE¹

¹*Department of Atmospheric and Oceanic Sciences, School of Physics, Peking University, Beijing 100871, China*

²*Aviation Meteorological Center, Civil Aviation Administration of China, Beijing 100122, China*

(Received 29 October 2019; revised 27 December 2019; accepted 28 January 2020)

ABSTRACT

Understanding the responses of mean and extreme precipitation to climate change is of great importance. Previous studies have mainly focused on the responses to prescribed sea surface warming or warming due to increases of CO₂. This study uses a cloud-resolving model under the idealization of radiative-convective equilibrium to examine the responses of mean and extreme precipitation to a variety of climate forcings, including changes in prescribed sea surface temperature, CO₂, solar insolation, surface albedo, stratospheric volcanic aerosols, and several tropospheric aerosols. The different responses of mean precipitation are understood by examining the changes in the surface energy budget. It is found that the cancellation between shortwave scattering and longwave radiation leads to a small dependence of the mean precipitation response on forcings. The responses of extreme precipitation are decomposed into three components (thermodynamic, dynamic, and precipitation efficiency). The thermodynamic components for all climate forcings are similar. The dynamic components and the precipitation-efficiency components, which have large spreads among the cases, are negatively correlated, leading to a small dependence of the extreme precipitation response on the forcings.

Key words: climate forcing, mean precipitation, extreme precipitation

Citation: Ma, C. Y., W. Yuan, and J. Nie, 2020: Responses of mean and extreme precipitation to different climate forcing under radiative-convective equilibrium. *Adv. Atmos. Sci.*, **37**(4), <https://doi.org/10.1007/s00376-020-9236-1>. (in press)

Article Highlights:

- The responses of mean and extreme precipitation to different climate forcings are investigated using a cloud-resolving model.
- Cancellation between shortwave scattering and longwave radiation leads to a small dependence of the mean precipitation response on forcings.
- Cancellation between the dynamic and precipitation-efficiency components leads to a small dependence of the extreme precipitation response on forcings.

1. Introduction

The response of the hydrological cycle to global warming is one of the key topics in climate research. The mean precipitation sensitivity (MPS, i.e., the fractional change in mean precipitation with 1°C of surface warming) is constrained by the radiative energy budget. Results from global climate models (GCMs) indicate a rate of about 2–3% K⁻¹ for the MPS for warming caused by increases in greenhouse gases (GHGs; Allen and Ingram, 2002; Held and Soden, 2006; O’Gorman and Schneider, 2008). There is, however, no apparent constraint for extreme precipitation sensitivity (EPS, i.e., the fractional change in extreme precipit-

ation with 1°C of surface warming). It has been argued that the increase in extreme precipitation may roughly follow the increase in atmospheric water vapor, which is ~7% K⁻¹ according to the Clausius–Clapeyron (CC) relation (Allen and Ingram, 2002; Trenberth et al., 2003; Kharin et al., 2007). GCM simulations show that the EPS has remarkable regional patterns, with over 30% K⁻¹ in some tropical regions and negative EPS in some subtropical regions, mainly due to the change in vertical ascent (Emori and Brown, 2005; Pfahl et al., 2017). Simple CC scaling is not enough to explain the EPS, and other factors need to be considered.

The majority of previous studies on the hydrological responses to climate changes have focused on GHG-induced warming, particularly for EPS studies. While anthropogenic CO₂ is the primary cause of current global warming, there is also a variety of climate forcings that may cause or contrib-

* Corresponding author: Ji NIE
Email: jinie@pku.edu.cn

ute to climate change. For example, atmospheric aerosols, either from natural sources such as volcano eruptions or from anthropogenic emissions, can affect atmospheric radiation directly and indirectly by changing cloud properties (Albrecht, 1989; Robock, 2000; Myhre et al., 2013). Changes in surface type can alter the surface albedo (Myhre et al., 2013). Solar insolation has an 11-year cycle, and over the geological time scale it has increased by about 20% from the Archean Eon (~2.7 billion years ago) (Kasting, 2010). Changes in deep-ocean circulation, which operates on a time scale of several thousands of years or longer, can induce surface energy flux anomalies to the atmosphere, which may also be viewed as climate forcing. Because the above-mentioned climate forcings affect the climate system's energy budget in different ways, they may result in different hydrological responses.

There are several possible reasons why the hydrological response may depend on the nature of the climate forcing. Firstly, the vertical profiles of the radiative forcing of the climate forcing are different. The GHG forcing increases the longwave emissivity; changes in insolation and albedo modify the shortwave flux at the top and bottom of the atmosphere, respectively; and the radiative forcing of aerosols depends on the properties and vertical profiles of aerosol concentrations. Secondly, in addition to direct radiative effects, aerosol can also affect cloud microphysics, which may further modify convection and precipitation processes (Grabowski, 2000; Wu, 2002). Thirdly, unlike the well-mixed GHGs, some climate forcings (e.g., aerosol forcing) are regional and may lead to different large-scale circulation anomalies. GCM simulations indicate that the MPS is different for the warming due to GHGs (1–3% K⁻¹), insolation (2.5–3.1% K⁻¹), and aerosols (3.7–3.8% K⁻¹) (Andrews et al., 2009; Ming et al., 2010; Shiogama et al., 2010; Frieler et al., 2011; Ming and Ramaswamy, 2011; Pendergrass and Hartmann, 2012; Boucher et al., 2013; Kvalevåg et al., 2013; Levy II et al., 2013). The dependence of EPS on climate forcing is inconclusive. Some studies have suggested that the EPS does not depend on the emissions scenario or driving force (Pendergrass et al., 2015; Sillmann et al., 2017), while others have indicated that the EPS due to aerosol forcing is significantly different from that caused by GHG forcing (Lin et al., 2016; Myhre et al., 2017). Furthermore, the EPSs for forcings other than GHGs and aerosols have not been explored.

The goal of this study is to investigate the responses of the hydrological cycle, including the MPS and EPS, to a variety of climate forcings. This problem is examined using a cloud-resolving model (CRM) under the idealization of radiative-convective equilibrium (RCE). CRMs, which are more reliable than GCMs in resolving convective-scale dynamics, have been shown to be a useful complement to GCMs in studies of the hydrological cycle (e.g., Held et al., 1993; Lau et al., 1993; Sui et al., 1994; Romps, 2011; Singh and O'Gorman, 2014; Nie et al., 2018). The idealization of RCE, which excludes the inhomogeneity in the surface condi-

tions and the large-scale circulations, provides a clean tested for our propose. Previous CRM studies have shown that the increase in extreme precipitation in response to surface warming is greater than that of the mean precipitation (Romps, 2011; Singh and O'Gorman, 2014). Muller et al. (2011) showed that the changes in vertical ascent contribute negatively to the EPS and cancel out the thermodynamic contributions from increases in atmospheric moisture. Muller (2013) further showed that the degree of convective organization may affect the EPS. However, most previous CRM studies have only considered GHG forcing or prescribed SST warming.

A variety of climate forcings are examined in this study, including changes in sea surface temperature (SST), CO₂, solar insolation, surface albedo, stratospheric aerosols, and tropospheric aerosols. As will be shown later, both the MPS and EPS show certain, but not large, dependence on the forcings. For the MPS, we examine the radiative budget to understand the different pathways of how the forcing affects mean precipitation. We show that, due to the cancellation between downward shortwave and downward longwave radiation, the MPS only weakly depends on the forcings. For the EPS, we apply a scaling method (O'Gorman and Schneider, 2009) to decompose the EPS into three components: dynamic, thermodynamic, and precipitation-efficiency components. Due to the cancellation between the effects of vertical ascent and precipitation efficiency, the EPS also only weakly depends on the forcings. The exception is black carbon (BC) forcing, which has a much smaller MPS and EPS than the other forcings. Section 2 introduces the numerical model and experimental design. Results are presented in section 3. Section 4 provides some discussion and summarizes our conclusions.

2. Model and experimental design

The model used here is the System of Atmospheric Modeling (Khairoutdinov and Randall, 2003), version 6.8. All simulations are run in a three-dimensional domain of 128 km × 128 km in the horizontal direction, with a resolution of 1 km. The vertical grid has 64 levels, with the grid spacing gradually increasing from 37.5 m at the surface to 500 m above 7 km. There are six water species in the microphysics scheme: water vapor, cloud liquid, cloud ice, snow, rain, and graupel. The interactive radiation scheme is from the National Center for Atmospheric Research Community Climate Model (Kiehl et al., 1998). A slab ocean of 0.5 m is used as the surface condition. The surface fluxes are interactively computed using Monin–Obukhov similarity theory.

Eight kinds of climate forcing are investigated in this study (Table 1), each with a pair of control and perturbed runs. The control runs of these experiments share the same settings (except the SST case): the CO₂ concentration is 355 ppm, and the insolation is set as annual mean values at 0°, without seasonal or diurnal variation, with a solar constant of 1367 W m⁻². All the aerosol species have zero concentra-

Table 1. The experimental designs in this study. The vertical profile of the volcanic aerosol added in the *Aer_str* experiment is shown in Fig. S1. The vertical profiles of the tropospheric aerosols added in the *Aer_tro*, *Aer_sul*, and *Aer_bc* experiments are shown in Fig. S2. In the *Aer_tro* experiment, the amplitude of the added aerosols is 20 times those in Fig. S2. In the *Aer_sul* experiment, the amplitude of the added sulfate aerosol is 30 times that in Fig. S2. In the *Aer_bc* experiment, the amplitude of the added black carbon aerosol is 200 times that in Fig. S2.

Experiment short name	Climate forcing	Change in SST	Mean precipitation sensitivity (% K ⁻¹)	Extreme precipitation sensitivity (% K ⁻¹)	Ranges of forcing magnitudes in reality
<i>SST</i>	Changing prescribed SST	+3.0K	4.7	6.7	~2K at end of the century under global warming (Myhre et al., 2013).
<i>CO₂</i>	Doubling CO ₂	+2.7K	3.9	5.4	An increase of ~200 ppm in the last century (Myhre et al., 2013).
<i>Ins</i>	Solar constant changes from 1367 to 1385 W m ⁻²	+3.1K	4.6	6.2	A variation of ~3 W m ⁻² for the 11-year solar cycle (Myhre et al., 2013); an increase of 270–350 W m ⁻² from the Archean Eon (2.7 billion years ago) to today (Kasting, 2010).
<i>Alb</i>	Surface albedo changes from 0.045 to 0.025.	+2.5K	4.8	6	The seasonal change of sea-ice albedo in the Arctic region is ~0.1, equivalent to a global albedo change of ~0.004 (Hummel and Reck, 1979).
<i>Aer_str</i>	Volcanic ash is added in the lower stratosphere (Fig. S1).	-2.5K	4.2	4.7	A global annual-mean total volcanic aerosol amount of ~4 Tg; a major eruption, such as the Samalas eruption in 1257–58, reaching ~160 Tg. (Liu et al., 2016).
<i>Aer_tro</i>	Tropospheric aerosol (11 species) is added in the troposphere (Fig. S2, with concentration multiplied by 20).	-3.1K	5.8	6.1	Annual anthropogenic aerosol emissions of 100–400 Tg yr ⁻¹ in the early 1970s and 300 Tg yr ⁻¹ in the 1990s (Gras, 2003).
<i>Aer_sul</i>	Sulfate added in the troposphere (Fig. S2, with concentration multiplied by 30).	-2.7K	5	5.9	Global annual-mean emissions of ~200 Tg yr ⁻¹ (Penner et al., 2001).
<i>Aer_bc</i>	BC added in the troposphere (Fig. S2, with concentration multiplied by 200).	+3.1K	-1.2	1.8	Global annual-mean emissions of about 4–8 Tg yr ⁻¹ (Bond et al., 2004).

tion. With the above insolation condition, the equilibrium SST will be much higher than our desired reference climate state. Thus, similar to the treatment in Romps (2011), a downward heat flux of 95 W m⁻² is applied at the bottom of the slab ocean to cool the equilibrium SST to be 299.6 K. The imposed flux sink may be viewed as heat moving into the deeper ocean and then being transported to higher latitudes by ocean circulation. In the *SST* experiment, the control run has a prescribed SST of 299.6 K.

Next, we introduce the perturbed runs. In the *SST* experiment, the perturbed run has a prescribed SST of 302.6 K. Note that the prescribed *SST* experiment does not conserve energy for the surface. For the other experiments, the SST is calculated interactively with the slab ocean. In these experiments (except the *SST* case), the magnitude of forcing in the perturbed runs is chosen so that the changes of equilibrium SST are around 3 K. In the perturbed run of the *CO₂* experiment, the CO₂ concentration is doubled, leading to a warming of SST by 2.7 K. In the perturbed run of the *Ins* experiment, the solar constant is increased to 1385 W m⁻². In the perturbed run of the *Alb* experiment, the surface albedo is de-

creased to 0.025 (compared with 0.045 in the control run). There are nine aerosol species (eight tropospheric aerosols and one stratospheric aerosol) in System of Atmospheric Modeling (Table S1 in Electronic Supplementary Material, ESM). All the tropospheric aerosols only have shortwave radiative effects, and the stratospheric (volcano) aerosol (75% sulfuric acid and 25% water) has both shortwave and longwave effects. In the perturbed run of the *Aer_str* experiment, volcanic aerosol is added in the lower stratosphere (Fig. S1 in ESM) to mimic the effects of major volcano eruptions. The magnitude of the added volcanic aerosol is 1×10^5 Tg, which is about 600 times that of a major volcanic eruption such as Samalas (Liu et al., 2016). The *Aer_tro* experiment is designed to examine the effects of tropospheric aerosols. The vertical distributions of the tropospheric aerosols are the global and annual-mean profiles from a GCM study (Fig. S2; Kipling et al., 2016). To reach a large SST difference of 3.1 K, the added aerosol concentrations are 20 times larger than the GCM results shown in Fig. S2. Additional experiments are performed to examine the individual effects of two representative tropospheric aerosols: sulfate aero-

sol (the *Aer_sul* experiment), which has a strong scattering effect on shortwave radiation; and BC (the *Aer_bc* experiment), which has a strong absorbing effect on shortwave radiation. Note that the magnitude of forcing in the two runs is also tuned accordingly, to have an SST change of about 3 K. All the runs are integrated for more than 1000 days, so that a statistical equilibrium is reached. As an example, several key domain-mean variables and cloud variables of the control and perturbed runs of the CO_2 case are shown in Fig. S3 and Fig. S4. The domain-mean variables are sampled every 5 min and the 3D snapshots are sampled every 6 h for the last 250 days (total of 72 000 samples of means and 1000 samples of 3D snapshots).

The responses of the hydrological cycle are calculated by taking the differences between the perturbed run and the control run in each pair of experiments. Extreme precipitation is defined as the surface precipitation rate at the 99.9th percentiles with all grid points considered (including grids with zero precipitation). For the five cases of *SST*, *CO₂*, *Ins*, *Alb*, and *Aer_bc* (called group 1 hereafter), the perturbed runs have warmer SST than the control runs. For the other three cases of *Aer_str*, *Aer_tro*, and *Aer_sul* (called group 2), adding these aerosols cools the SST. For better comparison, all the results are normalized by the SST changes. Thus, the results of cases in group 2 should be interpreted as removing aerosols from a background state of zero (this is justified if the hydrological response is nearly linear for small perturbations).

3. Results

3.1. Mean precipitation sensitivity

We first examine the changes in basic thermodynamic variables driven by different forcings (Fig. 1). The atmospheric temperature (T) increases with surface warming (Fig. 1a). The upper troposphere warms more than the lower troposphere does, because convection maintains the temperature profiles close to the moist adiabatic, which has a lapse rate decreasing with warming. For all the cases except that of *Aer_bc*, the δT values are close to each other, especially in the lower troposphere due to the strong constraint of moist convection. The outlier, the *Aer_bc* case, has significantly larger δT due to the strong shortwave absorbing in the lower troposphere. The changes in specific humidity (δq , Fig. 1b) are proportional with δT following the CC relationship. Throughout most of the troposphere, the cloud fraction decreases with warming (Fig. 1c). The cloud base moves downward slightly, and the cloud top moves upward in association with upper-tropospheric warming. This is consistent with previous studies (Bretherton, 2015; Vogel et al., 2016). Focusing on the tropopause layer, for the cases in group 1, the surface warming is associated with increases in tropopause height and cooling at the stratosphere (Fig. 1d), due to a rising of the effective emitting level (Vallis et al., 2015). For the cases in group 2 (*Aer_str* and *Aer_tro*, and *Aer_sul*), the aerosol perturbations induce radiative heating

at the upper-troposphere–lower-stratosphere, leading to warm responses there. As a result, the tropopause height slightly decreases in these cases. The differences suggest that different radiative effects of perturbations may cause different adjustments of tropopause height.

With CO_2 doubling, the mean precipitation increases $3.9\% K^{-1}$ (Table 1), consistent with previous CRM studies (Müller et al., 2011; Romps, 2011). The MPS in CRM simulations is larger than the results of GCMs ($2\text{--}3\% K^{-1}$), presumably partly due to the lack of large-scale circulation in the CRM, and partly due to the relatively high control SST here. For the other cases, the MPS ranges from $4.2\% K^{-1}$ (the *Aer_str* case) to $5.8\% K^{-1}$ (the *Aer_tro* case), except the outlier of the *Aer_bc* case, which shows a decrease in precipitation by $1.2\% K^{-1}$ (Table 1). To better understand the causes of the MPS differences among the cases, we use the surface energy budget framework (Roderick et al., 2014):

$$R_{Sd} + R_{Ld} - R_{Su} - R_{Lu} = H + E, \quad (1)$$

where R_{Sd}/R_{Su} is the surface downward/upward shortwave radiative flux, R_{Ld}/R_{Lu} is the surface downward/upward longwave flux, and H/E is sensible/latent heat flux. The variables in Eq. (1) are anomalies between the perturbed and the control runs. Since in the equilibrium state the precipitation is equal to the evaporation (i.e., the latent heat flux after unit conversion), Eq. (1) may be used to diagnose the MPS from the radiative energy perspective.

The results of the radiative energy budget are shown in Fig. 2a. The cases in group 1 show a decrease in downward shortwave flux (R_{Sd}), mainly due to the enhanced scattering effect associated with increased water vapor. In the *Aer_bc* case, the strong shortwave absorption by BC further heavily reduces R_{Sd} . The cases in group 2 have positive or zero R_{Sd} . Remember that the results of these cases should be thought of as removing aerosols from the control state (the last paragraph in section 2). Removal of the shortwave scattering aerosols (e.g., dust and sulfate) leads to increases in R_{Sd} . The changes in upward shortwave flux (R_{Su}) are small overall, except for the *Alb* case in which the decreased albedo reduces the surface reflection of shortwave radiation. The changes in net shortwave flux ($R_S = R_{Sd} - R_{Su}$) have a range of $-1.74 W m^{-2} K^{-1}$ to $1.47 W m^{-2} K^{-1}$ among the cases, except *Aer_bc*, which has an R_S of $-8.27 W m^{-2} K^{-1}$.

The changes in upward longwave flux (R_{Lu}) have very similar values ($\sim 6 W m^{-2} K^{-1}$) for all the cases. This is consistent with the theoretical estimation from the black-body radiation of $4\sigma T_s^3$ (taking surface temperature $T_s = 300 K$, this gives a value of $6.1 W m^{-2} K^{-1}$). The changes in downward longwave flux (R_{Ld}) have larger differences among the cases, dominating the variations of R_L . We have confirmed that the changes in net shortwave and longwave radiation are mainly due to the clear-sky radiation, while the contribution from the changes in cloud is small (Fig. 2b). The changes in sensible heat flux (H) are negligible, except for the *Aer_bc* case in which the increase in surface-layer air temperature reduces the temperature differences between the sur-

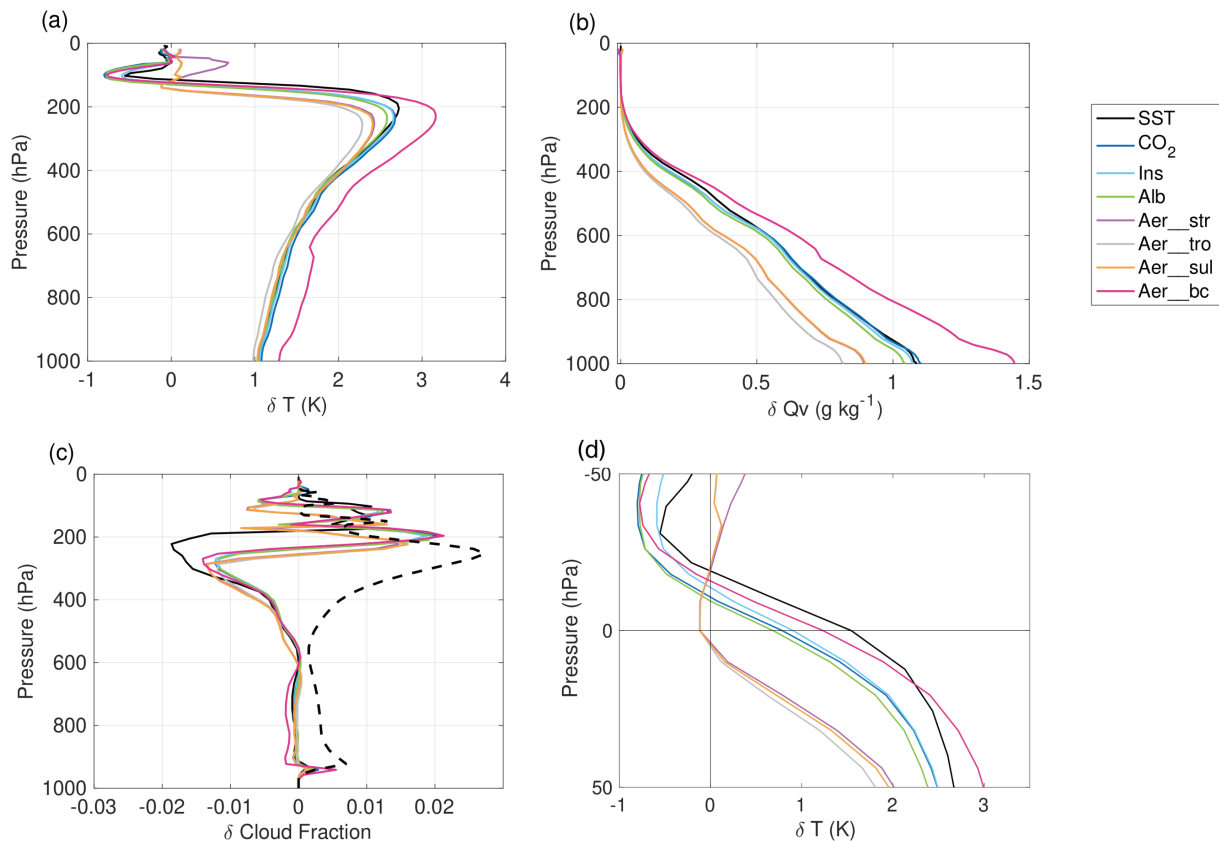


Fig. 1. The changes in (a) temperature, (b) specific humidity, (c) cloud fraction, and (d) temperature near the tropopause with unit surface warming. The black dashed line in (c) is the control run cloud fraction profile (divided by five to share the same x -axis as the anomalous profiles). In (d), the y -axis is the pressure above (positive) and below (negative) the tropopause of the control run.

face air and the surface, leading to a decrease in the sensible heat flux.

The above surface energy budget analysis suggests a strong negative correlation between R_{Sd} and R_{Ld} through the linkage of atmospheric temperature changes (δT). A larger δT is associated with a greater δq , and thus a stronger scattering of shortwave radiation and a more negative R_{Sd} (Fig. 3a). On the other hand, a warmer atmosphere sends more long-wave radiation back to the surface, resulting in a more positive R_{Ld} (Fig. 3b). The δT used in Fig. 3 is sampled at the 630-hPa level, because the above argument applies in the lower troposphere where water vapor is abundant and long-wave backward radiation is strong. Results with other, lower tropospheric levels also show high correlation. As the δT level increases, their correlation decreases, but it is still significant. The cancellation between R_S and R_L leads to a relatively weak dependence of the MPS on the forcings examined here. The exception is the BC forcing, in which the absorption by BC is superimposed on the scattering of water vapor, leading to a very strong reduction in downward shortwave radiation reaching the surface and a decrease in precipitation.

3.2. Extreme precipitation sensitivity

The EPS is greater than the MPS for all kinds of forcing (Table 1). The EPS ranges from 4.7% K^{-1} to 6.7% K^{-1}

among all the cases except the outlier of the *Aer_bc* case, which has an EPS of 1.8% K^{-1} . Due to the small temporal and spatial scale, precipitation extremes are not constrained by any long-term energy budget. Instead, dynamic and cloud microphysics can play important roles in determining the EPS (Muller et al., 2011; Singh and O’Gorman, 2014).

We use a scaling of precipitation extremes (O’Gorman and Schneider, 2009; Muller et al., 2011) to understand the dependence of the EPS on forcing. This scaling approximates precipitation extremes (P_e) with

$$P_e = -\varepsilon \left\{ \omega_e \frac{dq^*}{dp} \Big|_{\theta_e^*} \right\}, \quad (2)$$

where p is the pressure, $(dq^*/dp)|_{\theta_e^*}$ is the vertical material derivative of the saturation specific humidity at a constant saturation equivalent potential temperature (θ_e^*), ω_e is the vertical pressure velocity conditioned on the extreme-precipitation grids, and $\{\dots\}$ denotes the integral from the surface to the tropopause. The difference between the domain-mean temperature and temperature conditioned on extreme-precipitation grids is very small (Muller et al., 2010); thus, we use domain-mean temperature in the calculation of $(dq^*/dp)|_{\theta_e^*}$. ε is a precipitation-efficiency factor, with a value of 1 meaning that all the net condensates precipitate out (Muller et al., 2010). ε will depend on the cloud and precipitation microphys-

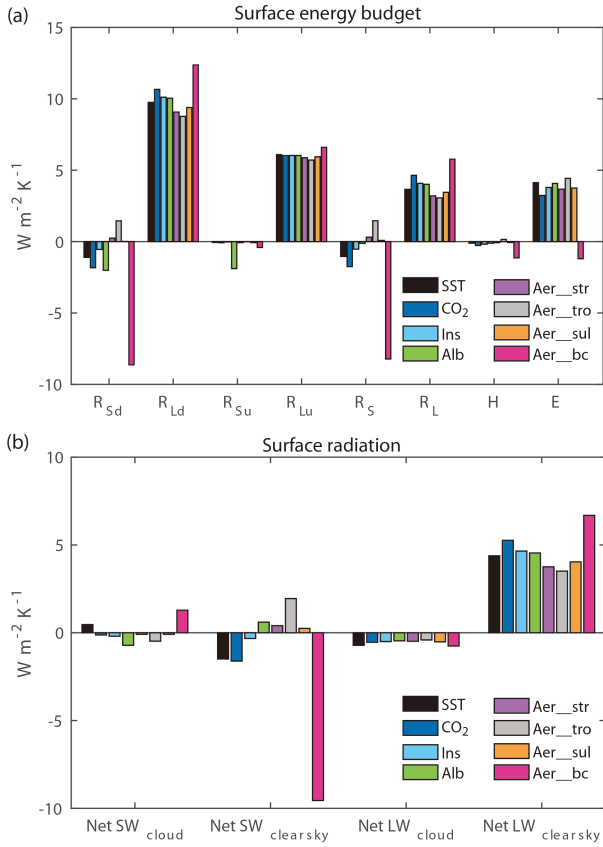


Fig. 2. (a) Perturbation analyses of the surface energy budget based on Eq. (1). (b) Separation of R_S and R_L into clear-sky and cloudy components.

ics (e.g., Wu, 2002; Singh and O’Gorman, 2014); however, in our calculation, ε is calculated diagnostically using model-output P_e . Future work should link the diagnosed ε with representations of cloud and precipitation microphysics, assigning a more explicit meaning to the precipitation-efficiency factor ε . For small perturbations of climate states, the fractional changes in P_e may be written as

$$\frac{\delta P_e}{P_e} = \frac{\left\{ \omega \delta \left(\frac{dq^*}{dp} \right) \Big|_{\theta_e^*} \right\}}{\left\{ \omega \frac{dq^*}{dp} \Big|_{\theta_e^*} \right\}} + \frac{\left\{ \delta(\omega) \frac{dq^*}{dp} \Big|_{\theta_e^*} \right\}}{\left\{ \omega \frac{dq^*}{dp} \Big|_{\theta_e^*} \right\}} + \frac{\delta \varepsilon}{\varepsilon}. \quad (3)$$

In Eq. (3), δ denotes differences between the perturbed and control runs of each experiment. The right-hand-side terms of Eq. (3) represent three components of EPS, which are the thermodynamic component (the increases in saturation water vapor), the dynamic component (the changes in vertical velocity), and the component due to the changes in precipitation efficiency. Note that the $\delta\varepsilon/\varepsilon$ term is neglected in the previous study by Muller et al. (2011) because it is small for GHG forcing. However, our numerical simulations show that, for other climate forcings, the $\delta\varepsilon/\varepsilon$ term is not negligible. Note that the $\delta\varepsilon/\varepsilon$ term is diagnosed here. It includes both the contribution of cloud and precipitation microphysics to the EPS and higher-order cross terms between the components in Eq. (2).

The decomposition of EPS based on Eq. (3) is shown in Fig. 4. The thermodynamic components for all cases are similar, with values around 10% K⁻¹. Under RCE, the changes of temperature profiles are closely tied to SST changes following moist adiabatic profiles (Fig. 1a). Thus, δT and the thermodynamic components ($(dq^*/dp)|_{\theta_e^*}$) of these cases are very close to each other. The Aer_{bc} case has a larger δT , corresponding to a larger thermodynamic component. Overall, the differences among the thermodynamic components are relatively small and do not explain the spread of EPSs.

The dynamic component is negative for all the cases (Fig. 4), with a sizeable spread. The key to understanding the dynamic component is the changes in vertical ascent during extreme precipitation. The changes in ω_e (Fig. 5a) show that the amplitude of ω_e in the middle troposphere decreases, and the level of the ω_e peak shifts upward. Although these cases share common features with a previous study (Muller et al., 2011) of GHG forcing, the amplitude of the ω_e changes is different, leading to different dynamic components. The weakening of vertical ascent largely explains

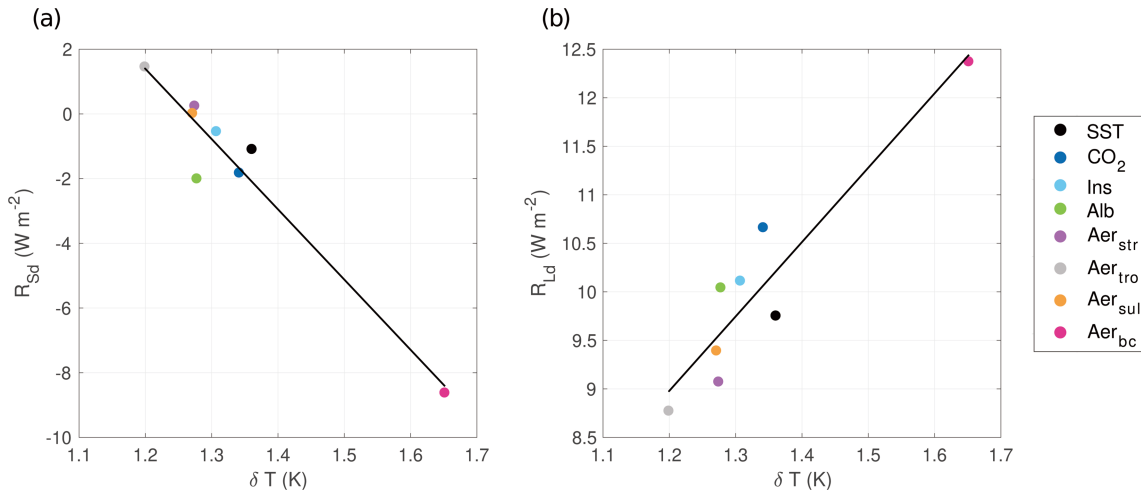


Fig. 3. Correlations between (a) δT at 630 hPa and R_{Sd} , and (b) δT at 630 hPa and R_{Ld} , of all the cases.

the dynamic component, as shown by the high correlation between the dynamic components and the changes in 500-hPa ω_e (Fig. 5b). The above analysis with $\delta\omega_e$, although able to explain the dynamic component diagnostically, has a fundamental limitation insofar as it requires information (ω_e) on the extreme-precipitation grids. For lower-resolution models, such as GCMs, the convective-scale processes

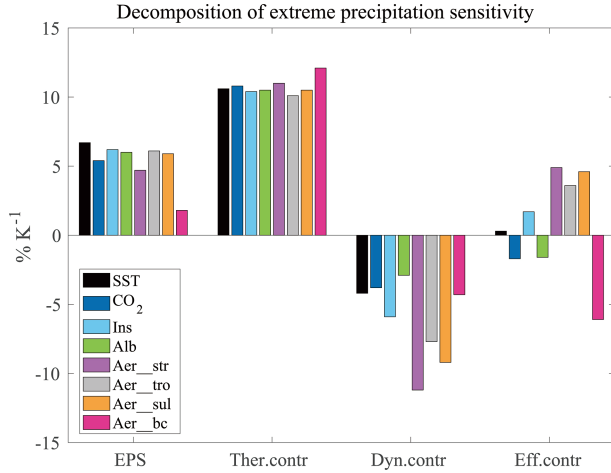


Fig. 4. The decomposition of EPS based on Eq. (3).

are not explicitly resolved, meaning these convective-scale variables are unavailable. Here, we move one step further to link the dynamic component to the larger-scale (i.e., CRM domain-mean) variables. It is found that there is a strong negative correlation between the dynamic components of the EPS and the changes in tropopause pressure (Fig. 5c), suggesting the effect of ω_e change is related to the change in tropopause height. This is consistent with a qualitative argument based on the convective plume perspective that, as the tropopause level rises, the convective available potential energy increases, tending to enhance convective ascent (Singh et al. 2014 2017). For the cases in group 2, the tropopause levels slightly decrease (Fig. 1d), corresponding to large negative dynamic components of EPS (Fig. 4).

Lastly, the precipitation efficiency component of EPS also has large variations. This component is negatively correlated with the dynamic component (Fig. 5d), so that the total EPS has relatively small variations. This negative correlation may be understood as follows: Given the time scale for the conversion of cloud-water condensation to precipitation is nearly unchanged with warming, the faster the convective updrafts ascend, the less time it takes for cloud updrafts to reach the cloud top, and the smaller the portion of cloud liquid water that can be converted into rainfall. Due to this can-

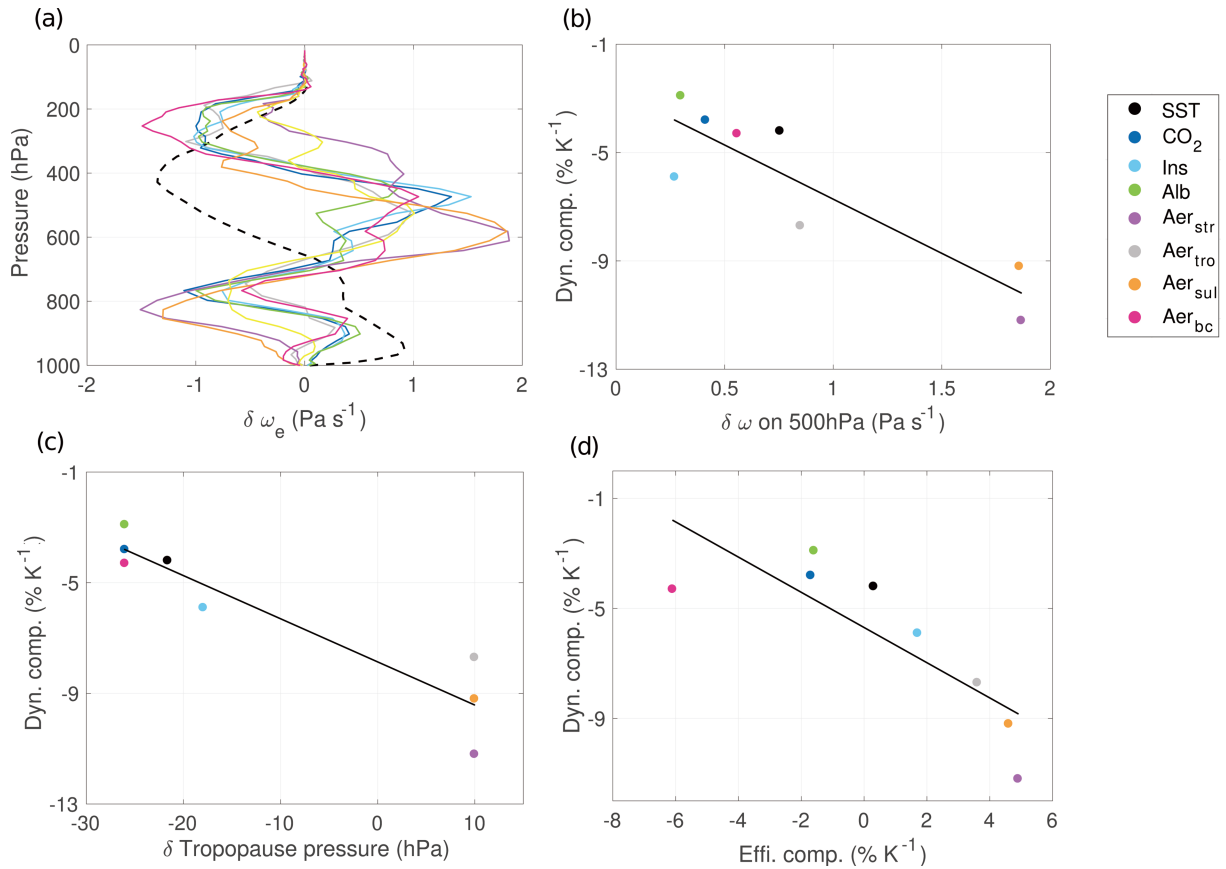


Fig. 5. (a) $\delta\omega_e$ (the changes in pressure velocity conditioned on extreme precipitation to unit surface warming). The black dashed line in (a) is the ω_e of the control runs (rescaled by dividing it by 10 for better visualization). (b) Scatterplot of $\delta\omega_e$ at 500 hPa and the dynamic components of EPS. (c) Scatterplot of changes in tropopause pressure and the dynamic components of EPS. (d) Scatterplot of the precipitation-efficiency components and the dynamic components of EPS.

cellation effect, the EPS is not very sensitive to different climate forcings under RCE in our CRM simulations.

4. Discussion and conclusions

This paper has examined the responses of mean and extreme precipitation to warming due to a variety of climate forcings in a CRM under RCE. When the concentration of CO₂ is doubled, the increase in mean precipitation is 3.9% K⁻¹, which roughly agrees with previous CRM studies (Muller et al., 2011; Romps, 2011). Other climate forcings, including prescribed SST, solar insolation, surface albedo, stratospheric volcanic aerosols, and tropospheric aerosols, lead to increases ranging from 4.2% K⁻¹ to 5.8% K⁻¹, except the case of BC forcing, which has a slight decrease in mean precipitation. The different responses of mean precipitation are understood by examining the changes in the surface energy budget. The surface warming is associated with a warmer and moister atmosphere. The surface downward shortwave flux decreases due to the stronger scattering effect associated with more abundant water vapor, while the surface downward longwave flux increases because of the warmer atmosphere. The negative correlation between shortwave and longwave radiation flux at the surface narrows the mean precipitation differences among the cases. In the BC forcing case, the strong absorption of shortwave radiation by BC causes a large reduction in surface downward shortwave flux that exceeds the increases in backward longwave radiation, leading to a decrease in mean precipitation by 1.2% K⁻¹. The EPS is greater than the MPS for all forcings. The change in extreme precipitation is decomposed into three components: the thermodynamic, dynamic, and precipitation-efficiency components. The thermodynamic components are similar among all the cases, since they are strongly constrained by the SST changes. The dynamic components are negative for all cases, with large variation. The changes in vertical velocity profiles show weakening in the middle troposphere and upward shifts of peaks. The dynamic components are correlated with the shifts in tropopause levels among the cases. The precipitation-efficiency component is negatively correlated with the dynamic component, presumably due to the constraint of the time scale of the conversion of cloud water to precipitation. The cancellation between the dynamic and precipitation-efficiency components leads to a small dependence of extreme precipitation on forcings.

The idealization of RCE removes the impacts of large-scale circulation changes on the MPS and EPS. An additional pair of experiments with imposed large-scale ascent (section S1) implies that the large-scale ascent drives the MPS approaching the CC scaling. The large-scale ascent also amplifies the EPS. However, further study is required to better survey the effects of large-scale motion on mean and extreme precipitation responses (Lau et al., 1993; Sui et al., 1994; Wu and Moncrieff, 1999). Besides, this study only considers the direct radiative effects of aerosol forcing and neglects the impacts of aerosols on cloud microphysics. The

main conclusion suggests that changing the radiative flux in different ways is not likely to generate large differences in the MPS and EPS, due to the cancellation mechanism discussed above. The exception is absorption of shortwave radiation in the atmosphere (i.e., the BC forcing), since the other forcing considered here may be thought of as the surface warming leading to atmospheric warming, while the *Aer_bc* case warms the surface by warming the atmosphere. The results of this study also suggest that the discrepancies in the dependence of the EPS on climate forcing in GCM studies (e.g., Pendergrass et al., 2015; Lin et al., 2016; Myhre et al., 2017; Sillmann et al., 2017) are more likely due to the different treatments of cloud microphysics. Further efforts on reducing the uncertainties of the impact of aerosol on cloud microphysics will benefit our understanding of how mean and extreme precipitation respond to climate change.

Acknowledgements. The authors thank the two anonymous reviewers and the editor for their valuable reviews, as well as Qiang FU and Qian CHEN for discussion. This research was supported by the National Natural Science Foundation of China (Grant No. 41875050).

Electronic supplementary material Supplementary material is available in the online version of this article at <https://doi.org/10.1007/s00376-020-9236-1>.

REFERENCES

- Albrecht, B. A., 1989: Aerosols, cloud microphysics, and fractional cloudiness. *Science*, **245**, 1227–1230, <https://doi.org/10.1126/science.245.4923.1227>.
- Allen, M. R., and W. J. Ingram, 2002: Constraints on future changes in climate and the hydrologic cycle. *Nature*, **419**, 228–232, <https://doi.org/10.1038/nature01092>.
- Andrews, T., P. M. Forster, and J. M. Gregory, 2009: A surface energy perspective on climate change. *J. Climate*, **22**, 2557–2570, <https://doi.org/10.1175/2008JCLI2759.1>.
- Bond, T. C., D. G. Streets, K. F. Yarber, S. M. Nelson, J. H. Woo, and Z. Klimont, 2004: A technology-based global inventory of black and organic carbon emissions from combustion. *J. Geophys. Res.*, **109**, D14203, <https://doi.org/10.1029/2003JD003697>.
- Boucher, O., and Coauthors, 2013: Clouds and aerosols. *Climate Change 2013: The Physical Science Basis. Contribution of Working Group I to the Fifth Assessment Report of the Intergovernmental Panel on Climate Change*, T. F. Stocker et al., Eds., Cambridge University Press, 571–657, <http://doi.org/10.1017/CBO9781107415324.016>.
- Bretherton C. S., 2015: Insights into low-latitude cloud feedbacks from high-resolution models. *Philos. Trans. Roy. Soc. London*, **373**, <https://doi.org/10.1098/rsta.2014.0415>.
- Emori, S., and S. J. Brown, 2005: Dynamic and thermodynamic changes in mean and extreme precipitation under changed climate. *Geophys. Res. Lett.*, **32**, L17706, <https://doi.org/10.1029/2005GL023272>.
- Frieler, K., M. Meinshausen, T. S. Von Deimling, T. Andrews, and P. Forster, 2011: Changes in global-mean precipitation in response to warming, greenhouse gas forcing and black car-

- bon. *Geophys. Res. Lett.*, **38**, L04702, <https://doi.org/10.1029/2010GL045953>.
- Grabowski, W. W., 2000: Cloud microphysics and the tropical climate: Cloud-resolving model perspective. *J. Climate*, **13**, 2306–2322, [https://doi.org/10.1175/1520-0442\(2000\)013<2306:CMATTC>2.0.CO;2](https://doi.org/10.1175/1520-0442(2000)013<2306:CMATTC>2.0.CO;2).
- Gras, J. L., 2003: AEROSOLS | climatology of tropospheric aerosols. *Encyclopedia of Atmospheric Sciences*, J. R. Holton, Ed., Academic Press, 13–20, <https://doi.org/10.1016/B0-12-227090-8/00051-8>.
- Held, I. M., and B. J. Soden, 2006: Robust responses of the hydrological cycle to global warming. *J. Climate*, **19**, 5686–5699, <https://doi.org/10.1175/JCLI3990.1>.
- Held, I. M., R. S. Hemler, and V. Ramaswamy, 1993: Radiative-convective equilibrium with explicit two-dimensional moist convection. *J. Atmos. Sci.*, **50**, 3909–3927, [https://doi.org/10.1175/1520-0469\(1993\)050<3909:RCEWET>2.0.CO;2](https://doi.org/10.1175/1520-0469(1993)050<3909:RCEWET>2.0.CO;2).
- Hummel, J. R., and R. A. Reck, 1979: A global surface albedo model. *J. Appl. Meteorol.*, **18**, 239–253, [https://doi.org/10.1175/1520-0450\(1979\)18\[239:AGSAM\]2.0.CO;2](https://doi.org/10.1175/1520-0450(1979)18[239:AGSAM]2.0.CO;2).
- Kasting, J., 2010: *How to Find a Habitable Planet*. Princeton University Press, 326pp.
- Khairoutdinov, M. F., and D. A. Randall, 2003: Cloud resolving modeling of the ARM summer 1997 IOP: Model formulation, results, uncertainties, and sensitivities. *J. Atmos. Sci.*, **60**, 607–625, [https://doi.org/10.1175/1520-0469\(2003\)060<0607:CRMOTA>2.0.CO;2](https://doi.org/10.1175/1520-0469(2003)060<0607:CRMOTA>2.0.CO;2).
- Kharin, V. V., F. W. Zwiers, X. B. Zhang, and G. C. Hegerl, 2007: Changes in temperature and precipitation extremes in the IPCC ensemble of global coupled model simulations. *J. Climate*, **20**, 1419–1444, <https://doi.org/10.1175/JCLI4066.1>.
- Kiehl, J. T., J. J. Hack, G. B. Bonan, B. A. Boville, D. L. Williamson, and P. J. Rasch, 1998: The national center for atmospheric research community climate model: CCM3. *J. Climate*, **11**, 1131–1149, [https://doi.org/10.1175/1520-0442\(1998\)011<1131:TNCFAR>2.0.CO;2](https://doi.org/10.1175/1520-0442(1998)011<1131:TNCFAR>2.0.CO;2).
- Kipling Z., and Coauthors, 2016: What controls the vertical distribution of aerosol? Relationships between process sensitivity in HadGEM3-UKCA and inter-model variation from AeroCom Phase II. *Atmospheric Chemistry and Physics*, **16**, 2221–2241, <https://doi.org/10.5194/acp-16-2221-2016>.
- Kvalevåg, M. M., B. H. Samset, and G. Myhre, 2013: Hydrological sensitivity to greenhouse gases and aerosols in a global climate model. *Geophys. Res. Lett.*, **40**, 1432–1438, <https://doi.org/10.1002/grl.50318>.
- Lau, K. M., C. H. Sui, and W. K. Tao, 1993: A preliminary study of the tropical water cycle and its sensitivity to surface warming. *Bull. Amer. Meteorol. Soc.*, **74**, 1313–1321, [https://doi.org/10.1175/1520-0477\(1993\)074<1313:APSOTT>2.0.CO;2](https://doi.org/10.1175/1520-0477(1993)074<1313:APSOTT>2.0.CO;2).
- Levy II, H., L. W. Horowitz, M. D. Schwarzkopf, Y. Ming, J. C. Golaz, V. Naik, and V. Ramaswamy, 2013: The roles of aerosol direct and indirect effects in past and future climate change. *J. Geophys. Res.*, **118**, 4521–4532, <https://doi.org/10.1002/jgrd.50192>.
- Lin, L., Z. L. Wang, Y. Y. Xu, and Q. Fu, 2016: Sensitivity of precipitation extremes to radiative forcing of greenhouse gases and aerosols. *Geophys. Res. Lett.*, **43**, 9860–9868, <https://doi.org/10.1002/2016GL070869>.
- Liu, F., J. Chai, B. Wang, J. Liu, X. Zhang, and Z. Y. Wang, 2016: Global monsoon precipitation responses to large volcanic eruptions. *Sci. Rep.*, **6**, 24331, <https://doi.org/10.1038/srep24331>.
- Ming, Y., and V. Ramaswamy, 2011: A model investigation of aerosol-induced changes in tropical circulation. *J. Climate*, **24**, 5125–5133, <https://doi.org/10.1175/2011JCLI4108.1>.
- Ming, Y., V. Ramaswamy, and G. Persad, 2010: Two opposing effects of absorbing aerosols on global mean precipitation. *Geophys. Res. Lett.*, **37**, L13701, <https://doi.org/10.1029/2010GL042895>.
- Muller, C., 2013: Impact of convective organization on the response of tropical precipitation extremes to warming. *J. Climate*, **26**, 5028–5043, <https://doi.org/10.1175/JCLI-D-12-00655.1>.
- Muller, C. J., P. A. O’Gorman, and L. E. Back, 2011: Intensification of precipitation extremes with warming in a cloud-resolving model. *J. Climate*, **24**, 2784–2800, <https://doi.org/10.1175/2011JCLI3876.1>.
- Myhre, G., and Coauthors, 2013: Anthropogenic and natural radiative forcing. *Contribution of Working Group I to the Fifth Assessment Report of the Intergovernmental Panel on Climate Change*, T. F. Stocker et al., Eds., Cambridge University Press, 659–740, <https://doi.org/10.1017/CBO9781107415324.018>.
- Myhre, G., and Coauthors, 2017: PDRMIP: A Precipitation Driver and Response Model Intercomparison Project-Protocol and Preliminary Results. *Bull. Amer. Meteor. Soc.*, **98**, 1185–1198, <https://doi.org/10.1175/BAMS-D-16-0019.1>.
- Nie, J., A. H. Sobel, D. A. Shaevitz, and S. G. Wang, 2018: Dynamic amplification of extreme precipitation sensitivity. *Proc. Natl. Acad. Sci. USA*, **115**, 9467–9472, <https://doi.org/10.1073/pnas.1800357115>.
- O’Gorman, P. A., and T. Schneider, 2008: The hydrological cycle over a wide range of climates simulated with an idealized GCM. *J. Climate*, **21**, 3815–3832, <https://doi.org/10.1175/2007JCLI2065.1>.
- O’Gorman, P. A., and T. Schneider, 2009: The physical basis for increases in precipitation extremes in simulations of 21st-century climate change. *Proc. Natl. Acad. Sci. USA*, **106**, 14773–14777, <https://doi.org/10.1073/pnas.0907610106>.
- Pendergrass, A. G., and D. L. Hartmann, 2012: Global-mean precipitation and black carbon in AR4 simulations. *Geophys. Res. Lett.*, **39**, L01703, <https://doi.org/10.1029/2011GL050067>.
- Pendergrass, A. G., F. Lehner, B. M. Sanderson, and Y. Y. Xu, 2015: Does extreme precipitation intensity depend on the emissions scenario? *Geophys. Res. Lett.*, **42**, 8767–8774, <https://doi.org/10.1002/2015GL065854>.
- Penner, J. E., and Coauthors, 2001: Aerosols, their direct and indirect effects. *Contribution of Working Group I to the Third Assessment Report of the Intergovernmental Panel on Climate Change*, J. T. Houghton et al., Eds., Cambridge University Press, 289–348.
- Pfahl, S., P. A. O’Gorman, and E. M. Fischer, 2017: Understanding the regional pattern of projected future changes in extreme precipitation. *Nat. Clim. Change*, **7**, 423–427, <https://doi.org/10.1038/nclimate3287>.
- Robock, A., 2000: Volcanic eruptions and climate. *Rev. Geophys.*, **38**, 191–219, <https://doi.org/10.1029/1998RG000054>.
- Roderick, M. L., F. Sun, W. H. Lim, and G. D. Farquhar, 2014: A general framework for understanding the response of the water cycle to global warming over land and ocean. *Hydrology and Earth System Sciences*, **18**, 1575–1589, <https://doi.org/10.5194/hess-18-1575-2014>.

- Romps, D. M., 2011: Response of tropical precipitation to global warming. *J. Atmos. Sci.*, **68**, 123–138, <https://doi.org/10.1175/2010JAS3542.1>.
- Shiogama, H., and Coauthors, 2010: Emission scenario dependencies in climate change assessments of the hydrological cycle. *Climatic Change*, **99**, 321–329, <https://doi.org/10.1007/S10584-009-9765-1>.
- Sillmann, J., C. W. Stjern, G. Myhre, and P. M. Forster, 2017: Slow and fast responses of mean and extreme precipitation to different forcing in CMIP5 simulations. *Geophys. Res. Lett.*, **44**, 6383–6390, <https://doi.org/10.1002/2017GL073229>.
- Singh, M. S., and P. A. O’Gorman, 2014: Influence of microphysics on the scaling of precipitation extremes with temperature. *Geophys. Res. Lett.*, **41**, 6037–6044, <https://doi.org/10.1002/2014GL061222>.
- Singh, M. S., Z. M. Kuang, E. D. Maloney, W. M. Hanna, and B. O. Wolding, 2017: Increasing potential for intense tropical and subtropical thunderstorms under global warming. *Proc. Natl. Acad. Sci. USA*, **114**, 11657–11662, <https://doi.org/10.1073/pnas.1707603114>.
- Sui, C. H., K. M. Lau, W. K. Tao, and J. Simpson, 1994: The tropical water and energy cycles in a cumulus ensemble model. Part I: Equilibrium climate. *J. Atmos. Sci.*, **51**, 711–728, [https://doi.org/10.1175/1520-0469\(1994\)051<0711:TTWAEC>2.0.CO;2](https://doi.org/10.1175/1520-0469(1994)051<0711:TTWAEC>2.0.CO;2).
- Trenberth, K. E., A. G. Dai, R. M. Rasmussen, and D. B. Parsons, 2003: The changing character of precipitation. *Bull. Amer. Meteorol. Soc.*, **84**, 1205–1217, <https://doi.org/10.1175/BAMS-84-9-1205>.
- Vallis, G. K., P. Zurita-Gotor, C. Cairns, and J. Kidston, 2015: Response of the large-scale structure of the atmosphere to global warming. *Quart. J. Roy. Meteorol. Soc.*, **141**, 1479–1501, <https://doi.org/10.1002/qj.2456>.
- Vogel, R., L. Nuijens, and B. Stevens, 2016: The role of precipitation and spatial organization in the response of trade-wind clouds to warming. *Journal of Advances in Modeling Earth Systems*, **8**, 843–862, <https://doi.org/10.1002/2015MS000568>.
- Wu, X. Q., 2002: Effects of ice microphysics on tropical radiative-convective-oceanic quasi-equilibrium states. *J. Atmos. Sci.*, **59**, 1885–1897, [https://doi.org/10.1175/1520-0469\(2002\)059<1885:EOIMOT>2.0.CO;2](https://doi.org/10.1175/1520-0469(2002)059<1885:EOIMOT>2.0.CO;2).
- Wu, X. Q., and M. W. Moncrieff, 1999: Effects of sea surface temperature and large-scale dynamics on the thermodynamic equilibrium state and convection over the tropical western Pacific. *J. Geophys. Res.*, **104**, 6093–6100, <https://doi.org/10.1029/1998JD200116>.

**Electronic Supplementary Material to:
Responses of Mean and Extreme Precipitation to Different Climate
Forcings Under Radiative-Convective Equilibrium
Supplementary Information**

Chenyu MA¹, Wei YUAN², and Ji NIE^{*1}

¹*Department of Atmospheric and Oceanic Sciences, School of Physics, Peking University, Beijing 100871, China*

²*Aviation Meteorological Center, Civil Aviation Administration of China, Beijing 100122, China*

ESM to : Ma, C. Y., W. Yuan, and J. Nie, 2020: Responses of mean and extreme precipitation to different climate forcing under radiative–convective equilibrium. *Adv. Atmos. Sci.*, **32**(4), <https://doi.org/10.1007/s00376-020-9236-1>. (in press)

Supplementary Figures

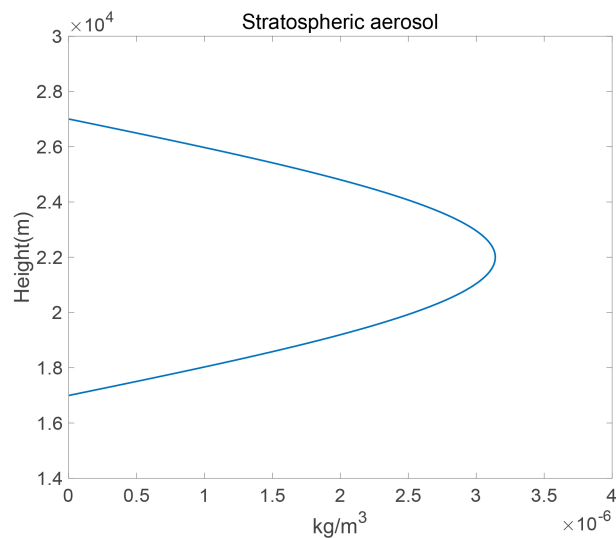


Fig. S1. The vertical profile of volcanic aerosol added in the *Aer_str* experiment. The vertical profile is half sinusoidal with a width of 10 km centred at 8 km above the tropopause.

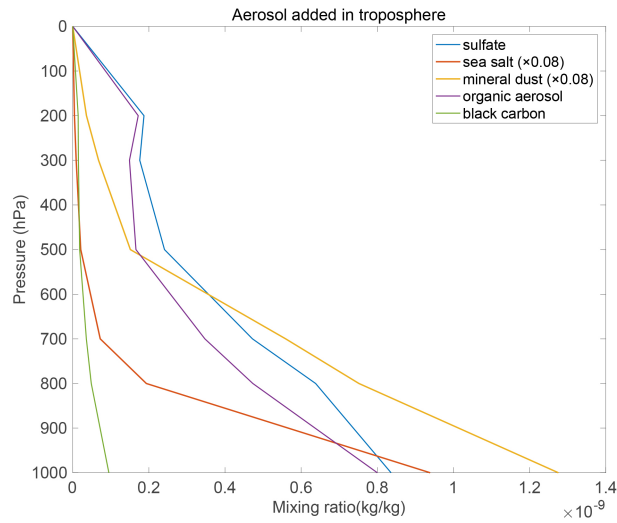


Fig. S2. The vertical profiles of tropospheric aerosols added in the *Aer_tro*, *Aer_sul*, and *Aer_bc* experiments. The vertical profiles are taken from the global mean and annual mean of a GCM study (Zak Kipling et al. 2016). The concentrations of sea salt and mineral dust are significantly larger than the others. For sharing the same x-axis, the values of sea salt and mineral dust concentrations are multiplied by 0.08 (this is only for the purpose of illustration).

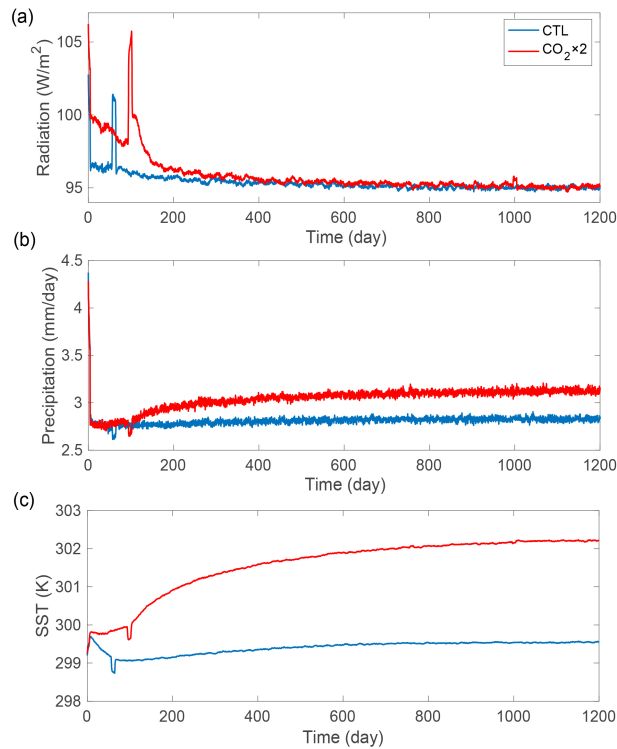


Fig. S3. The time series of (a) net top-of-atmosphere (TOA) radiation flux, (b) precipitation, and (c) SST of the control run (blue lines) and the perturbed run (red lines) of the CO_2 case. At the end of the simulation, the system has reached a statistical equilibrium state. There is a net downward TOA radiation flux of 95 W m^{-2} , corresponding to the prescribed flux transported into the deep ocean.

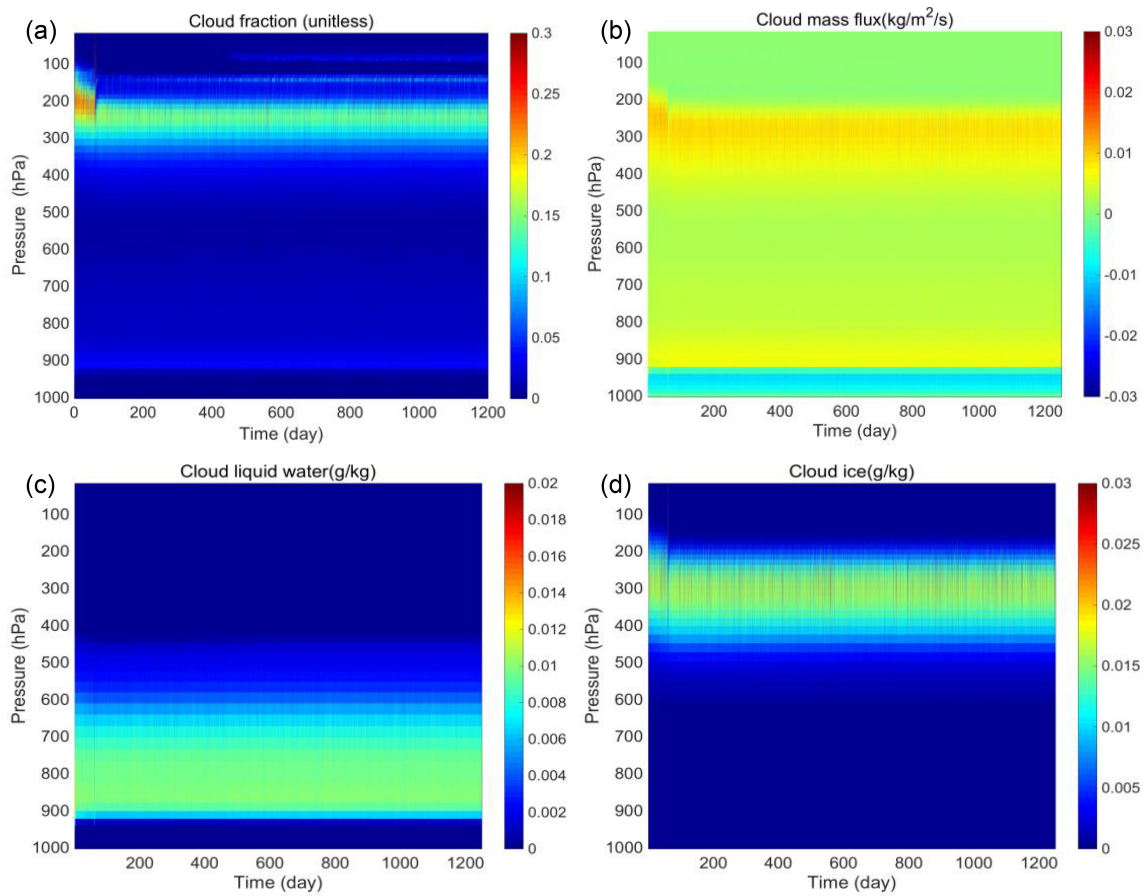


Fig. S4. Temporal evolution of the vertical profiles of the (a) cloud fraction, (b) cloud mass flux, (c) cloud liquid water, and (d) cloud ice of the control run of the CO_2 case.

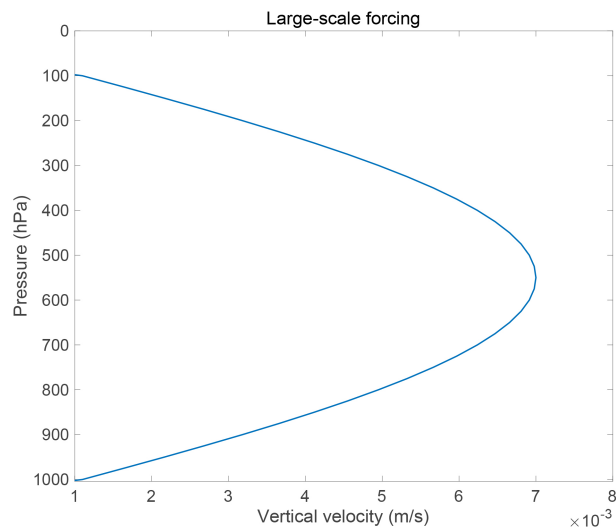


Fig. S5. Vertical profile of the imposed large-scale ascent. The profile is a half cosine function between the surface and 100 hPa. Results of the simulations with imposed large-scale ascent are described in section S1.

Supplementary Tables

Table 1. The aerosol species in SAM and their radiative effects.

Species type	Aerosol	Radiative effects
Species 1	Sulfate	Very strong shortwave scattering
Species 2	Sea salt	Very strong shortwave scattering
Species 3–6	Mineral dust in four bins with different diameters	Very strong shortwave scattering
Species 7	Organic carbon	Very strong shortwave scattering
Species 8	Black carbon	Very strong shortwave absorption
Species 9	Stratospheric aerosol (75% sulfuric acid + 25% water)	Sulfuric acid has very strong shortwave scattering effect. Water vapor has very strong longwave absorption effect.

Supplementary Section

S1. Effects of large-scale vertical motion on mean and extreme precipitation sensitivity

Here we describe the results of a pair of experiments conducted to briefly explore the effects of large-scale vertical motion on mean and extreme precipitation sensitivity. The pair of experiments is the same as the *SST* case, except prescribed large-scale vertical ascent (Fig. S5) is imposed on both the control run and the perturbed run.

Let us consider the mean precipitation and its responses. The imposed large-scale ascent induces vertical advection of moisture, which is an additional source term that has to be balanced by precipitation in the equilibrium state. From the vertical profile of ascent (Fig. S5) and moisture, it is estimated that the large-scale term corresponds to precipitation of about 5.4 mm d⁻¹, leading to mean precipitation of 8.1 mm d⁻¹ in the control case (Table S2). With surface warming, the atmospheric moisture increases at a rate approximately following the Clausius–Clapeyron scaling (~7% K⁻¹). Given the same large-scale ascent, precipitation due to the large-scale motion will also increase following the CC scaling. This rate is higher than the precipitation due to convection along (~4% K⁻¹; results in the main text). Thus, the increasing rate of mean precipitation is within the range from 4% K⁻¹ to 7% K⁻¹, consistent with the simulation results (Table S2). If a stronger large-scale ascent is imposed, the contribution of the large-scale term to mean precipitation increases, and the mean precipitation sensitivity will further approach the CC scaling of 7% K⁻¹. The results here are consistent with previous studies (Lau et al. 1993; Sui et al. 1994; Wu and Moncrieff 1999).

Since there is no energy constraint for the extreme precipitation, we cannot make a prognostic scaling of extreme precipitation sensitivity as we did for the mean precipitation sensitivity. Simulation results (Table S2) show that with the imposed large-scale ascent, the intensity of extreme precipitation increases significantly, compared to the cases without the imposed large-scale ascent. The imposed ascent moistens the free troposphere, invigorating convection and precipitation. The responses of extreme precipitation to surface warming is 8.6% K⁻¹, greater than that of the *SST* case without large-scale ascent and even greater than the CC scaling. It suggests strong positive feedback of moisture to extreme precipitation (e.g., Nie et al., 2018). The results here indicate that the extreme precipitation sensitivity depends on the large-scale vertical motion, which is qualitatively consistent with the fact that in reality there are significant geographic variations of extreme precipitation sensitivity. The results described in the main text need modifications when the large-scale vertical motion is included in the system.